



Morphology regulation and electrochemical properties of cathode material V_6O_{13} for lithium-ion battery

Xin Liu¹ · Zhengguang Zou¹ · Jianying Meng¹ · Shuchao Zhang¹ · Shenglin Zhong¹ · You Li¹

Received: 4 December 2021 / Revised: 9 March 2022 / Accepted: 11 March 2022 / Published online: 17 March 2022
© The Author(s), under exclusive licence to Springer-Verlag GmbH Germany, part of Springer Nature, corrected publication 2022

Abstract

A V_6O_{13} micro-flower was synthesized via a facial hydrothermal method using ammonium metavanadate and oxalic acid dihydrate and combined with subsequent heat treatment. The effects of oxalic acid concentration and subsequent calcination temperature on the crystallinity and microstructure of V_6O_{13} are discussed in detail. We have compared these data to determine the optimal amount of reducing agent and calcination temperature and further explored the electrochemical properties of cathode materials. The results show that the concentration of oxalic acid and calcination temperature has a great influence on the morphology and crystallinity. When paired with Li anode, V_6O_{13} cathode exhibits excellent electrochemical performance that the initial specific capacity is 376.7 mA g^{-1} and the capacity retention of 48.3% after 100 cycles at the current density of 100 mA g^{-1} . This work provides some references for the development of high-performance lithium-ion battery cathodes.

Keywords V_6O_{13} · Morphology regulation · Cathode material · Lithium-ion battery

Introduction

Nowadays, there is a significant demand for rechargeable batteries with reversible and efficient electrochemical energy storage and conversion in the field of large-scale power storage in portable electronic consumer devices, electric vehicles, and smart grids [1]. Lithium-ion rechargeable battery has attracted much attention because of its large capacity, high power, and long cycle life. At the same time, it can also store clean energy from solar energy, wind energy, and so on [2, 3].

The metal lithium was taken as the negative electrode, for its very low electrode potential (-3.04 V , vs. standard hydrogen electrode) and a high specific capacity (3860 mAh g^{-1}) [4]. If a suitable positive electrode material that can accommodate lithium-ions can be found, obtaining a rechargeable lithium-ion battery with ideal voltage and energy density will be promising. At present, the commercial cathode materials mainly include LiCoO_2 , $\text{LiNi}_x\text{Co}_y\text{Mn}_z\text{O}_2$ (NCM), $\text{LiNi}_x\text{Co}_y\text{Al}_z\text{O}_2$ (NCA), LiMn_2O_4 , and LiFePO_4 . The capacity of these materials is generally lower than 250 mAh g^{-1} ,

which is far lower than that of cathode materials [5]. Hence, the research on high-capacity and high-performance cathode materials is absolutely significant for the development of lithium-ion batteries. The large interlayer of cathode material spacing provides sufficient space and smooth channels for the insertion and removal of lithium ions, which can significantly improve the movement (electrode dynamics) of lithium ions in the lattice, so as to improve the diffusion rate of lithium ions [6–8]. In recent years, vanadium oxides (VO_2 , V_2O_5 , V_6O_{13} , etc.) have attracted more and more attention, which are also considered a potential cathode material for reversible lithium-ion batteries due to their layered structure and high theoretical capacity [9, 10]. Among them, the V_6O_{13} mixed-valence state ($\text{V}^{4+}:\text{V}^{5+} = 2:1$) presents metal properties at room temperature and possesses the properties of high conductivity. In the redox process of V_6O_{13} , there are four cavities in each unit of V_6O_{13} between single layer and double layer, which will accommodate up to 8 mol of lithium ions, with a theoretical capacity of 420 mAh g^{-1} , theoretical specific energy of 900 Wh/kg and a working voltage of more than 1.5 V [11–13]. This unique layered structure and cavity in a specific direction make V_6O_{13} a promising cathode material for high-performance lithium-ion batteries. Although there have been many reports on the successful synthesis of V_6O_{13} , its theoretical capacity is still far below the theoretical capacity [14–16]. Therefore, it is meaningful to optimize

✉ Zhengguang Zou
zouzglut@163.com

¹ College of Materials Science and Engineering, Guilin University of Technology, Guilin, China

the experimental parameters to improve the purity of V_6O_{13} , which will significantly contribute to the actual capacity getting closer to the theoretical capacity.

There are many methods for the synthesis of V_6O_{13} , such as solid phase method, hydrothermal method, and sol–gel method. V_6O_{13} cathode material was synthesized by hydrothermal method in this experiment. The previous work of our research group has proved that V_6O_{13} synthesized by the hydrothermal method has better electrochemical performance, higher purity, and its morphology is more conducive to the intercalation of ions and the combination of conductive materials [17]. The parameters in the hydrothermal process have a great impact on the crystal form, morphology, and particle size of the products [18]. The calcination process will affect the particle size and tend to obtain a more ideal crystal structure. Consequently, not only the degree of cation mixing can be reduced, but also the products with required characteristics can be prepared, and the structure and electrochemical stability of cathode materials can be improved by controlling these factors. Li et al. [19] synthesized and calcined MoO_x nanoparticles as lithium-ion battery electrode materials at 600 °C, 700 °C, and 800 °C, respectively, in argon environment. According to BET analysis, the surface area increases from 96.1 to 259.3 $m^2 g^{-1}$ with the increase of calcination temperature, and the pore volume first increases and then decreases with the increase of calcination temperature. Seh-Yoon Lim [20] synthesized urchin-type hollow porous-structured VO_2 cathode material by controlling hydrothermal reaction time and calcination time, which proved that nucleation growth would affect the morphology and pore volume of nanorods. After hydrothermal reaction for 24 h and holding at 200 °C for 24 h, micelle-free nanorods were formed to aggregate urchin-type hollow porous VO_2 (B) structure. At 3C current density, the initial discharge specific capacity was 272 mAh g^{-1} , and the discharge specific capacity was 248 mAh g^{-1} after 200 cycles. Hayder A. Abbood et al. [1] synthesized the fabrication of cross-like $NH_4V_4O_{10}$ nanobelt array by hydrothermal method and investigated the effects of CMC concentration, pH value, and temperature on $NH_4V_4O_{10}$. The results show that the pH value in the reaction medium plays an important role in the morphology of the product. Through TGA analysis, the temperature affects the crystal growth, and the formation of mixed-valence state of vanadium atoms calcined at 400 °C is more conducive. He et al. [2] explored the effect of hydrothermal time on the product structure and grew a three-dimensional interconnected V_6O_{13} nest structure on carbon cloth. The analysis shows that the optimum condition is a hydrothermal reaction at 160 °C for 5 h. Since the optimization of experimental parameters to improve the electrochemical properties of materials is an effective method, the above experiments are crucial to explore and optimize experimental parameters and synthesize cathode materials with better electrochemical performance.

Our current target is to synthesize high specific capacity V_6O_{13} cathode material with better crystal structure through the adjustment of the oxalic acid concentration and calcination temperature by hydrothermal method. Previously, V_6O_{13} was synthesized by solvothermal method, hydrothermal method, and solid-phase method. However, according to XRD analysis, most samples contain a small amount of impurities such as VO_2 and V_2O_5 . Therefore, it is still a challenge to separate the mixed-valence single-phase compositions and explore the electrochemical properties of pure phase V_6O_{13} by formulating an elaborate synthesis protocol [18].

Experimental section

Synthesis of V_6O_{13}

Ammonium vanadate (NH_4VO_3 , Aladdin, 99.9%) and oxalic acid dihydrate ($C_2H_2O_4 \cdot 2H_2O$, Xilongs Science, AR) were used as raw materials, which were analytically pure. V_6O_{13} nano-architectures were synthesized by hydrothermal synthesis. A total of 0.8 g ammonium vanadate powder was added to 45 mL deionized water with a certain proportion of oxalic acid dihydrate. The solution was agitated constantly at room temperature for 2 h to form a green liquid. Next, the above solution was mixed evenly and was transferred it to a 63 mL of Teflon-lined autoclave for treatment at 160 °C for 24 h. After the reaction, wait for the auto-claves to cool down to an ambient temperature naturally and wash the precipitate with deionized water 3 times. The precipitate was pre-frozen for 3 h and then freeze-dried at -40 °C for 24 h. After the dried sample was ground evenly, the samples placed in a BEQ BTF-1200C-S tube furnace and were annealed under N_2 for 1 h (gas flow rate: 13–14 L/min). Sequently, the samples were heated to a certain temperature at 3 °C/min, and we could obtain the V_6O_{13} micro-flowers after the powder cooled down to an ambient temperature naturally. The samples were numbered V1, V2, V3, and V4 according to the molar ratios of ammonium vanadate and oxalic acid dihydrate which are 1/1, 4/5, 8/11, and 2/3.

Material characterization

X'pert pro X-ray diffractometer (XRD) produced by PANalytical was used to analyze the phase and determine the crystallinity of the material. S-4800 field emission scanning electron microscope (FESEM) was carried out by Hitachi and was used to analyze the morphology of the samples synthesized with different parameters. The microstructure and morphology of V_6O_{13} samples were analyzed by Philips JEM-2100F transmission electron microscope (TEM) and HRTEM. ESCALAB 250Xi X-ray photoelectron

spectroscopy (XPS) produced by Thermo Electron Corporation was used to analyze the molecular structure and elemental valence.

Electrochemical characterization

CR2025 coin-type cell was used to test the electrochemical properties of the prepared materials. According to the mass ratio of 7:2:1, the active substance (V_6O_{13} sample), battery grade acetylene carbon black, and binder (PVDF, AR) were added into the agate mortar; afterwards, the above substance was dissolved in an appropriate amount of N-methyl-2-pyrrolidone (NMP, AR) solvent and ground evenly. The mixed slurry was coated on the aluminum foil (thickness 150 μm), dried in an oven at 60 $^\circ\text{C}$ for 2 h, and then vacuum-dried at 90 $^\circ\text{C}$ for 12 h. The precision disc punching machine cuts the pole piece into circular electrode with a diameter of 16 mm as the positive electrode of the battery. CR2025 coin cell was assembled in a MIKROUNA Super glove box filled with high-purity argon ($\geq 99.999\%$), taking commercial lithium sheet as the negative electrode, polyethylene microporous membrane as the diaphragm, and 1.0 M LiPF₆ (EC:DMC = 3:7 vol%) as electrolyte. The charge and discharge performance of the battery was tested by the NEWARE CT-5 V-10 mA Battery Testing System at 25 $^\circ\text{C}$. The electrochemical measurements and the electrochemical impedance spectroscopy (EIS) were tested by CHI860D electrochemical workstation (scanning speed 0.1 mV s^{-1} ; scanning range 1.5–4.0 V).

Results and analysis

Figure 1 is the XRD spectrum of the powder prepared by different molar ratios of ammonium vanadate and oxalic acid dihydrate at the calcination temperature of 350 $^\circ\text{C}$. Compared with the standard card of V_6O_{13} (PDF # 89-0100), the V3 sample had almost no impurity peak, and a purer V_6O_{13} phase was obtained. The reduction process of the whole system can be considered $\text{NH}_4\text{VO}_3 \rightarrow \text{NH}_4\text{V}_4\text{O}_{10} \rightarrow \text{V}_6\text{O}_{13} \rightarrow 3\text{VO}_2$. The powder mainly presented $\text{NH}_4\text{V}_4\text{O}_{10}$ phase ($\text{V}^{4+}:\text{V}^{5+} = 1:2$), when the oxalic acid concentration is low. With the increase of oxalic acid dosage, V^{5+} was gradually over reduced to V^{4+} , and $\text{NH}_4\text{V}_4\text{O}_{10}$ phase was gradually converted to V_6O_{13} phase. When the molar ratio was 8:11, the crystal phase was mainly V_6O_{13} phase. When the molar ratio was higher than 8:11, NH_4VO_3 was overreduced and VO_2 phase began to appear, indicating that oxalic acid has been excessive at this time. We have experimented with more ratio about the ratio between ammonium vanadate and oxalic acid dihydrate, the XRD spectrum as shown in Fig. S1. $\text{NH}_4\text{V}_4\text{O}_{10}$ phase had a strong diffraction peak at 9.7 $^\circ$ and V_6O_{13} phase had a weak

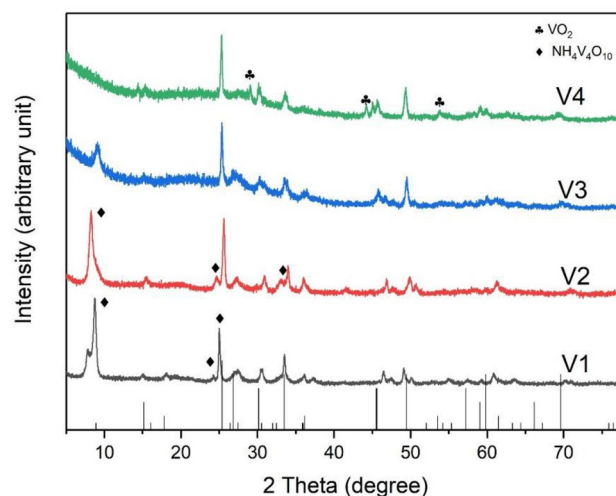


Fig. 1 X-ray diffraction pattern of as-synthesized powder as a function of oxalic acid concentration

diffraction peak at 8.9 $^\circ$. With the increase of oxalic acid concentration, it can be obviously observed that the double peak become a single peak near 9 $^\circ$ and the diffraction peak intensity decreased gradually. At the molar ratio of 8:11, the V3 sample was combined with a relatively pure V_6O_{13} phase, but it was still influenced by heterophase and needed further purification.

Figure 2 shows the SEM spectrum of the powder prepared with different molar ratios of ammonium vanadate and oxalic acid dihydrate at the calcination temperature of 350 $^\circ\text{C}$. The sample shows the micro-flower morphology composed of nanoribbons. Vanadium source and reducing agent were dissolved into aqueous solution under stirring conditions, and ammonium metavanadate was converted into VO_2^+ under acidic conditions, and VO_2^+ was complexed with $\text{C}_2\text{O}_4^{2-}$ ions to form layered complex ions $[(\text{VO}_2)_2(\text{C}_2\text{O}_4)_3]^{2-}$. Under acidic conditions, VO_2^+ has strong reducibility and partially oxidized oxalic acid to form VO^{2+} . At 160 $^\circ\text{C}$, the oxalic acid in the complex decomposed gradually with the increase of reaction time. Because of the Oswald ripening, the complex directional growth occurs, and “cluster nanobelts” are formed. After calcination, the “cluster nanobelts” further split to form a “like-flower structure” [21, 22]. With the increase of oxalic acid concentration, the size of the sample first decreased, then increased, and then decreased, and gradually formed a micro flower morphology.

However, the agglomeration of the sample became more serious with the decrease of particle size. The particles were obviously composed of several micro flowers, as shown in Fig. 2h. The size of nanoribbons became larger, and the micro flowers were more dispersed at the concentration ratio of ammonium vanadate to oxalic acid is 11:8, as shown in

Fig. 2 SEM of different concentration ratios of ammonium vanadate and oxalic acid at 350 °C. **a, b** V1: 1/1; **c, d** V2:4/5; **e, f** V3:8/11; and **g, h** V4:2/3

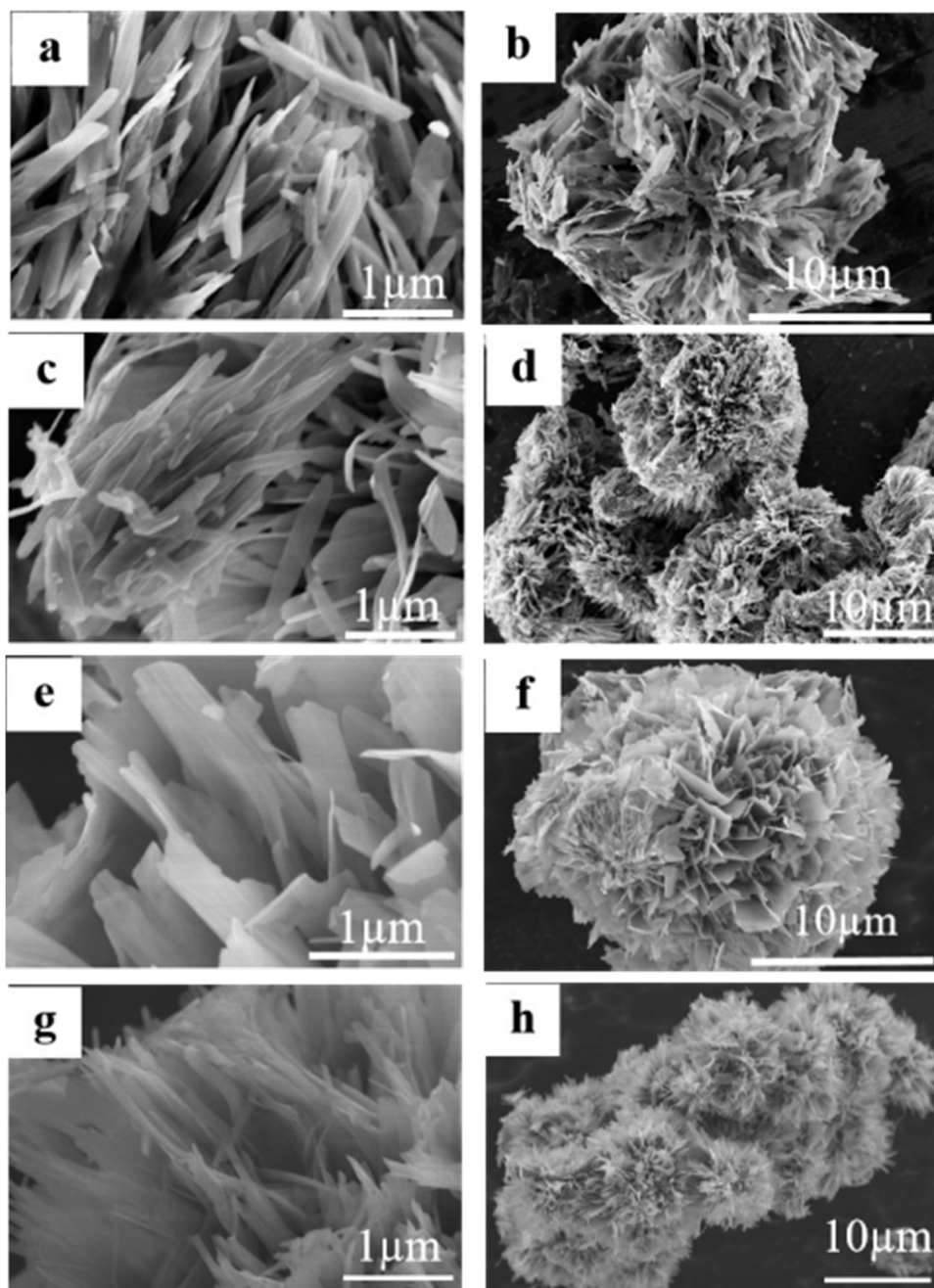


Fig. 2e and f. It can be seen that with the increase of oxalic acid concentration, the acidity and alkalinity of the reaction environment changed, which have a great effect on the preferred orientation and morphology of the sample [6]. In addition, oxalic acid as reducing agent will also affect the purity of V_6O_{13} . As analyzed by XRD, if the concentration was too low, the $NH_4V_4O_{10}$ will be formed, and if the concentration was too high, excessive reduction will lead to the formation of VO_2 . Therefore, since the oxalic acid worked as reducing agent and morphology control agent, the control of its concentration was very important for the formation of samples.

The following tests and analyses were carried out under the condition that the molar ratio of ammonium vanadate to oxalic acid dihydrate was 8:11. $NH_4V_4O_{10}$ calcined at 350 °C or above can decompose and release reducing gas ammonia, which led to pentavalent vanadium being reduced to a low valence state, and contribute to the formation of mixed valence V_6O_{13} micro-flower morphology [1, 14, 23]. Figure 3 is the XRD spectrum of the powder calcined at different temperatures. According to the analysis, the diffraction rays of the three samples were in good agreement with the standard card by comparing with the standard card of V_6O_{13} (PDF#89–0100). With the increase of calcination

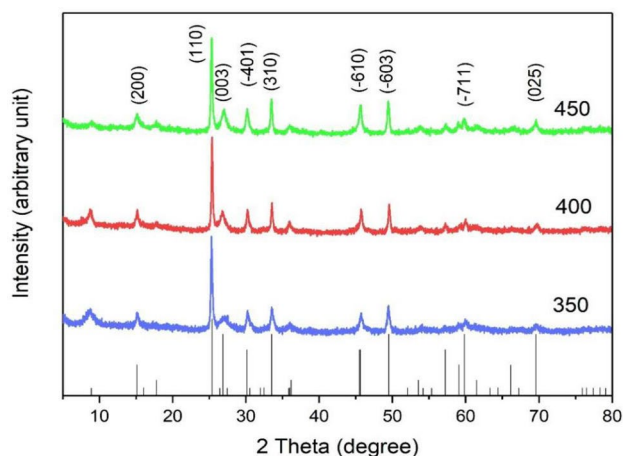


Fig. 3 X-ray diffraction pattern of V_6O_{13} material as a function of calcination temperature

temperature, the diffraction peak corresponding to the (110) crystal plane was sharp, indicating that the better crystallinity is obtained. It can be clearly observed in the diffraction

pattern that the diffraction peak at 26.8° became sharp with the increase of calcination temperature. The diffraction lines of the samples calcined at 400°C and 450°C are highly consistent with the standard card of V_6O_{13} (PDF#89–0100), indicating that V_6O_{13} is synthesized successfully.

Figure 4 is a SEM diagram of powders calcined at different temperatures. Figure 4a and b show the samples calcined at 350°C and micro-flowers with a diameter of about $20\ \mu\text{m}$, which are composed of nanoribbons with a width of about $270\ \text{nm}$; Fig. 4c and d show samples calcined at 400°C and micro-flowers with a diameter of about $14\ \mu\text{m}$, which are composed of nanoribbons with a width of about $120\ \text{nm}$. TEM images in Fig. 6a shows a clearer morphology. It can be seen that the width of an individual nanoribbons was $122\ \text{nm}$, which was consistent with the SEM analysis results; Fig. 4e and f show samples calcined at 450°C and micro-flowers with a diameter of about $20\ \mu\text{m}$, which were composed of nanoribbons with a width of about $100\ \text{nm}$. With the increase of calcination temperature, the size of nanoribbons decreased gradually. However, the size was too small, leading to the agglomeration aggravates, since the

Fig. 4 SEM of as-synthesized powder at different calcination temperature. a, b 350°C ; c, d 400°C ; and e, f 450°C

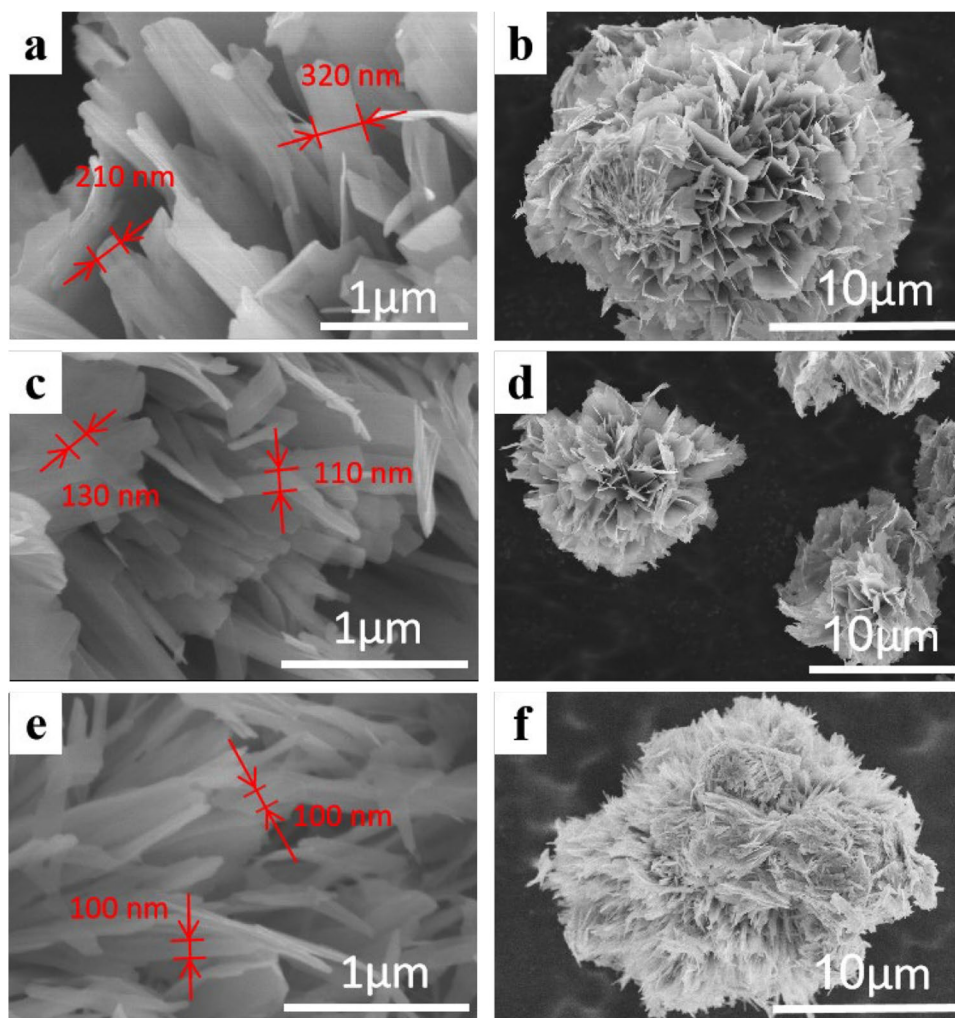
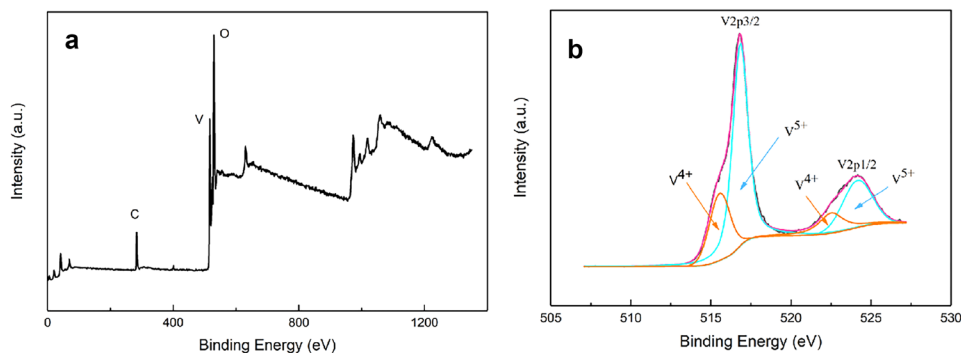


Fig. 5 **a** Overall elemental survey spectrum of V_6O_{13} . **b** High-resolution XPS spectrum of vanadium in V_6O_{13}



lithium-ion diffusion area reduces with the sharp increases of the size of particles. Therefore, it is not conducive to the electrochemical performance of V_6O_{13} . In order to observe the specific surface area and porosity of the material, the specific surface areas and pore size of three representative samples were characterized by N_2 adsorption and desorption measurements and shown in Fig. S2. The adsorption–desorption isotherm of N_2 was a typical IV isotherm with obvious hysteresis curve, indicating that V_6O_{13} cathode material had a meso-porous structure. With the increase of temperature, the specific surface area was $29.93 \text{ m}^2 \text{ g}^{-1}$, $34.12 \text{ m}^2 \text{ g}^{-1}$, and $24.58 \text{ m}^2 \text{ g}^{-1}$, respectively. It can be seen that the sample prepared at $400 \text{ }^\circ\text{C}$ has the largest specific surface area, and the high specific surface area can produce more lithium-embedded positions, which is conducive to the initial discharge capacity of the material closer to the theoretical value. The samples calcined at $400 \text{ }^\circ\text{C}$ had a regular arrangement, and small and dispersed micro-flower size not only shortens the distance of ion migration but also provides more redox reaction active sites. Therefore, it is judged that its electrochemical performance is the best [11, 24, 25]. Combined with SEM and BET results, we believe that the calcination temperature of $400 \text{ }^\circ\text{C}$ is the best experimental condition for the synthesis of V_6O_{13} cathode materials.

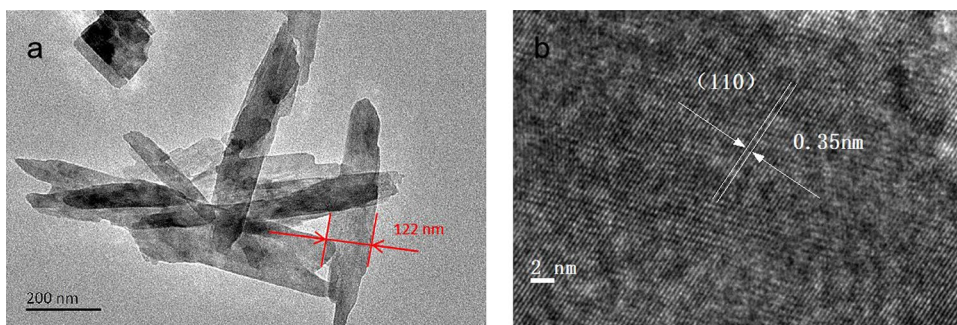
V_6O_{13} is a substance with mixed valence state. Herein, XPS analysis was carried out to analyze the element composition and oxidation state of the powder. Figure 5 is the X-ray photoelectron spectroscopy (XPS) of the synthetic powder calcined at $400 \text{ }^\circ\text{C}$. The main constituent elements of V_6O_{13}

are C, V, and O, as shown in Fig. 5a. The XPS spectrum of V2p is shown in Fig. 5b. The characteristic peaks with binding energies of 515.88 eV, 516.88 eV, 523.08 eV, and 524.58 eV correspond to $V^{4+}2p^{3/2}$, $V^{5+}2p^{3/2}$, $V^{4+}2p^{1/2}$, and $V^{5+}2p^{1/2}$ respectively. This confirms that there are two different oxidation states of vanadium in the crystal structure of V_6O_{13} [2, 26, 27]. It is observed in Fig. 5b that the peak area of V^{5+} was larger than that of V^{4+} . It may be that XPS mainly analyzed the element composition of the sample surface, and the test depth was shallow. The oxidation–reduction reaction tended to occur when the surface was in contact with the electrolyte, and V^{5+} was easy to be reduced on the surface.

Figure 6 shows TEM and HRTEM image of V_6O_{13} cathode material prepared at $400 \text{ }^\circ\text{C}$. Consistent with the SEM results, there was a nanosheet morphology as shown in Fig. 6a. Besides, Fig. 6b shows the lattice fringes of V_6O_{13} , and the lattice spacing of 0.35 nm corresponded to the (110) crystal plane of V_6O_{13} . Moreover, the results are compatible with those in the references [27, 28].

CR2025 coin-type cells were assembled with metal lithium sheet as negative electrode, and the electrochemical performance was tested which is shown in Fig. 7. The electrochemical impedance spectroscopy of cathode materials prepared at different calcination temperatures is shown in Fig. 7a. The Warburg factor (σ) of the sample has been calculated, and the alternating current impedance (resistance) as well as lithium-ion diffusion coefficient (D_{Li}) is shown in Table 1. The charge transfer resistances of the samples were 688.6Ω ($350 \text{ }^\circ\text{C}$), 628.8Ω ($400 \text{ }^\circ\text{C}$), and 630.6Ω ($450 \text{ }^\circ\text{C}$), respec-

Fig. 6 **a** High-magnification image of V_6O_{13} microstructure. **b** HRTEM image



tively. V_6O_{13} has metal properties at room temperature, so its charge transfer impedance was small [12]. Li^+ intercalation of VO_6 octahedral lattice will lead to lattice distortion, resulting in the destruction of V_6O_{13} crystal in the cycle process, and poor cycle performance. Therefore, the smaller the resistance value is, the more stable the cycle performance of cathode material is. The lithium-ion diffusion coefficients of the sample are shown in Fig. 7b and Table 1, with the maximum at 400 °C, the second at 350 °C, and the minimum at 450 °C. The results are consistent with the SEM images. It can be seen that the size of nanoribbons calcined at 450 °C was too small, and excessive agglomeration blocked the Li^+ diffusion channel, which was not conducive to the insertion and removal of Li^+ . Figure 7c shows the CV curve of the sample calcined at 400 °C which was acquired from an electrochemical workstation with a voltage between 1.5 and 4.0 V at a scanning rate of 0.1 mV s^{-1} . Two pairs of redox peaks can be observed, which is similar to other experimental results [25, 29, 30]. The second charge–discharge cycle curve is similar to the first one, with almost the same capacity, showing high reversible electrochemical properties, indicating that the sample calcined at 400 °C had good cycle stability.

The electrochemical performance of the three samples was further discussed through the cyclic test. The cyclic performance and first charge–discharge curve under 100 mA g^{-1} current density and 1.5–4.0 V voltage range are shown in Fig. 7d and e. The initial discharge specific capacities of

Table 1 Resistance, σ and D_{Li} values for different calcination temperature

Temperature (°C)	Resistance (Ω)	σ	D_{Li} ($\text{cm}^2 \text{ s}^{-1}$)
350	688.6	39.216	1.05×10^{-14}
400	628.8	34.398	1.37×10^{-14}
450	630.6	59.535	0.46×10^{-14}

samples calcined at 350 °C, 400 °C, and 450 °C were 365.2 mAh g^{-1} , 376.7 mAh g^{-1} , and 308.6 mAh g^{-1} at 100 mA g^{-1} current density, respectively. The discharge specific capacities after 100 cycles were 137.6 mAh g^{-1} , 181.9 mAh g^{-1} , and 131.3 mAh g^{-1} respectively, and the capacity retention rates were 37.6%, 48.3%, and 42.5%, respectively. The results show that the agglomeration of nanoribbons hinders the intercalation path of lithium ions, reduces the ions entering the lattice, and affects the specific discharge capacity of cathode materials. The internal resistance of the material itself is an important factor affecting the structural stability of the material. Hence, the sample calcined at 400 °C with the minimum internal resistance has the best cyclic stability. In Fig. 7e, all samples have obvious voltage platforms. The difference between the charge and discharge voltage platforms of the samples calcined at 350 °C was large, indicating the serious material polarization and the energy heavy loss. It is consist-

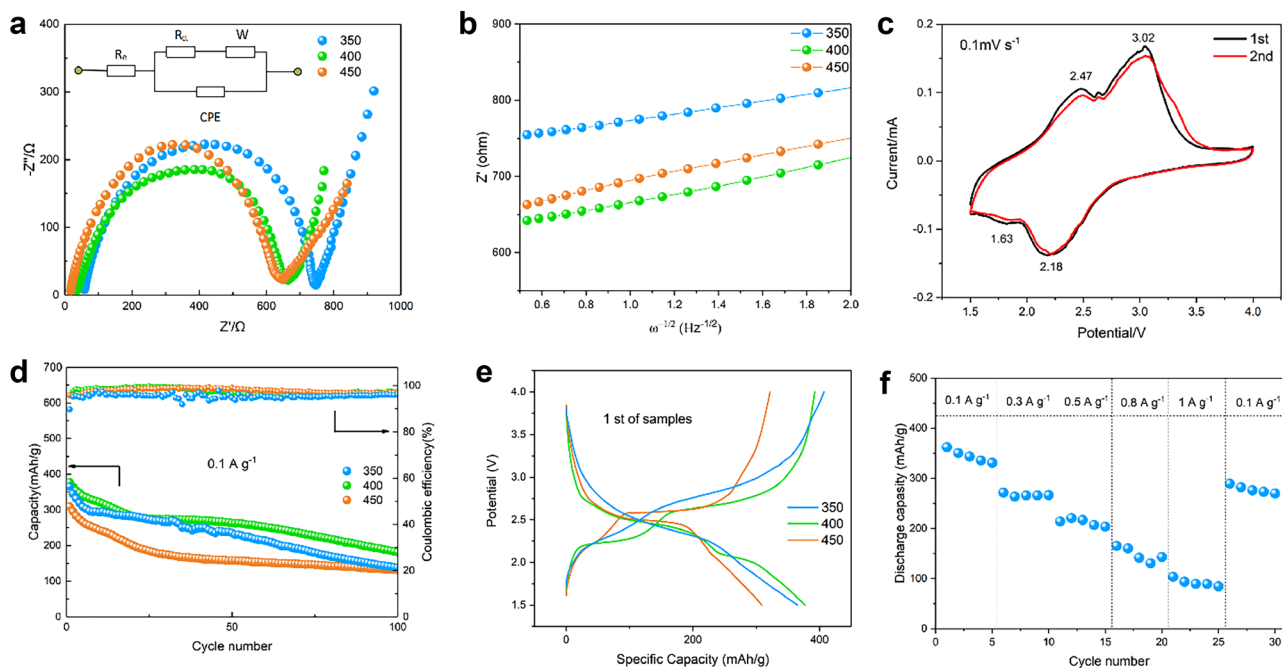


Fig. 7 **a** EIS impedance diagrams of samples and the insert shows the corresponding equivalent circuit. **b** The relation curves related to Z' vs. $\omega^{-1/2}$. **c** CV results for a cathode in a coin-type cell calcination at 400 °C. **d** Galvanostatic cyclic performances and corresponding cou-

lombic efficiencies of samples measured at 100 mA g^{-1} . **e** Discharge/charge profile of samples. **f** Rate capability performances of the V_6O_{13} calcination at 400 °C

ent with the results of the cycle performance diagram. The results show that a series of phase transitions occurs when lithium ions were intercalated/deintercalated from the crystal structure, resulting in chemical and structural changes. We disassembled the battery after 100 cycles, explored the structure changes of the cathode material calcinated at 400 °C after the cycle, and conducted SEM test as shown in Fig. S3. It is obvious that the material morphology after the cycle was seriously damaged, and many nanoribbons were crushed and split, by comparing the morphology before and after the cycle. To study the electrochemical performance of the material better, we studied the rate performance of the sample under the cyclic test current density of 100 mA g⁻¹, 300 mA g⁻¹, 500 mA g⁻¹, 800 mA g⁻¹, and 1000 mA g⁻¹ in the voltage range of 1.5–4.0 V, as shown in Fig. 7f. As the current density increased from 100 to 1000 mA g⁻¹, the discharge specific capacity decreased from 362 to 104 mAh g⁻¹, the current density returned to 100 mA g⁻¹, and the discharge specific capacity increased to 290 mAh g⁻¹. Because the layered vanadium oxides are composed of VO_x layers with weak intermolecular force interactions, frequent lithium-ion insertion/deinsertion easy causes volume change, structural damage, and collapse, resulting in rapid capacity attenuation [31].

A brief comparison of this work with some already reported work on V₆O₁₃ for LIB cathode. This has improved many performances than previously reported V₆O₁₃ cathode materials, as summarized in Table S1.

Conclusions

In this work, we synthesized the micro-flower-like V₆O₁₃ cathode material composed of nanoribbons by simple hydrothermal method. It is demonstrated that oxalic acid concentration and calcination temperature are two crucial factors for the synthesis of V₆O₁₃ micro-flower with high crystallinity. Under the optimal conditions of a molar ratio of ammonium metavanadate and oxalic acid of 8:11 and a calcination temperature of 400 °C, the V₆O₁₃ micro-flower had higher crystallinity and lower specific surface area, which provided more active sites. Based on the above advantages, the V₆O₁₃ cathode achieves the best electrochemical performance. When the current density was 100 mA g⁻¹, the initial discharge specific capacity was 376.7 mAh g⁻¹, and the capacity retention rate could reach 48.3% after 100 cycles. This work provides an insight for the development of high-performance lithium-ion battery.

Supplementary information The online version contains supplementary material available at <https://doi.org/10.1007/s10008-022-05151-9>.

Funding This work was supported by the National Natural Science Foundation of China (No. 51562006) and Guangxi Distinguished Experts Special Fund (No. 2019B06).

Declarations

Conflict of interest The authors declare no competing interests.

References

1. Abbood HA, Peng H, Gao X, Tan B, Huang K (2012) Fabrication of cross-like NH₄V₄O₁₀ nanobelt array controlled by CMC as soft template and photocatalytic activity of its calcinated product. *Chem Eng J* 209:245–254
2. He P, Liu J, Zhao X, Ding Z, Gao P, Fan L-Z (2020) A three-dimensional interconnected V₆O₁₃ nest with a V⁵⁺-rich state for ultrahigh Zn ion storage. *J Mater Chem A* 8(20):10370–10376
3. Qu X, Huang G, Xing B, Si D, Xu B, Chen Z, Zhang C, Cao Y (2019) Core-shell carbon composite material as anode materials for lithium-ion batteries. *J Alloys Compd* 772:814–822
4. Zhu B, Wang X, Yao P, Li J, Zhu J (2019) Towards high energy density lithium battery anodes: silicon and lithium. *Chem Sci* 10(30):7132–7148
5. Zhang H, Zhao H, Khan MA, Zou W, Xu J, Zhang L, Zhang J (2018) Recent progress in advanced electrode materials, separators and electrolytes for lithium batteries. *J Mater Chem A* 6(42):20564–20620
6. Sarkar S, Veluri PS, Mitra S (2014) Morphology controlled synthesis of layered NH₄V₄O₁₀ and the impact of binder on stable high rate electrochemical performance. *Electrochim Acta* 132:448–456
7. Hua K, Li X, Fang D, Bao R, Yi J, Luo Z, Fu Z, Hu J (2018) Vanadium trioxide nanowire arrays as a cathode material for lithium-ion battery. *Ceram Int* 44(10):11307–11313
8. Wang S, Qin J, Zhang Y, Xia F, Liu M, Chen H, Al-Mamun M, Liu P, Rigway R, Shi G, Song J, Zhong YL, Zhao H (2019) Tungsten-doped nanocrystalline V₆O₁₃ nanoparticles as low-cost and high-performance electrodes for energy storage devices. *Energy Technol* 7(8):1801041
9. Yang G, Wei T, Wang C (2018) Self-healing lamellar structure boosts highly stable zinc-storage property of bilayered vanadium oxides. *ACS Appl Mater Interfaces* 10(41):35079–35089
10. Yang W, Zeng J, Xue Z, Ma T, Chen J, Li N, Zou H, Chen S (2019) Synthesis of vanadium oxide nanorods coated with carbon nanoshell for a high-performance supercapacitor. *Ionics* 26(2):961–970
11. Tamilselvan M, Sreekanth TVM, Yoo K, Kim J (2020) Binder-free coaxially grown V₆O₁₃ nanobelts on carbon cloth as cathodes for highly reversible aqueous zinc ion batteries. *Appl Surf Sci* 529
12. Shan L, Zhou J, Zhang W, Xia C, Guo S, Ma X, Fang G, Wu X, Liang S (2019) Highly reversible phase transition endows V₆O₁₃ with enhanced performance as aqueous zinc-ion battery cathode. *Energy Technol* 7(6)
13. Lai J, Zhu H, Zhu X, Koritala H, Wang Y (2019) Interlayer-expanded V₆O₁₃·nH₂O architecture constructed for an advanced rechargeable aqueous Zinc-ion battery. *ACS Appl Energy Mater* 2(3):1988–1996
14. Tian X, Xu X, He L, Wei Q, Yan M, Xu L, Zhao Y, Yang C, Mai L (2014) Ultrathin pre-lithiated V₆O₁₃ nanosheet cathodes with enhanced electrical transport and cyclability. *J Power Sources* 255:235–241
15. Zhang Y, Meng C (2015) Facile one-pot hydrothermal synthesis of belt-like β-V₆O₁₃ with rectangular cross sections for Li-ion battery application. *Mater Lett* 160:404–407
16. Wu M, Zhu K, Liang P, Yao Z, Shi F, Zhang J, Yan K, Liu J, Wang J (2021) Uniform rotate hydrothermal synthesis of V₆O₁₃ nanosheets as cathode material for lithium-ion battery. *J Alloys Compd* 877.

17. Wu X, Zou Z, Li S, Wang Z (2019) Simple synthesis and electrochemical performance of V_6O_{13} cathode materials as lithium-ion batteries. *Ionics* 25(3):1413–1418
18. Mutta GR, Popuri SR, Ruterana P, Buckman J (2017) Single step hydrothermal synthesis of mixed valent V_6O_{13} nano-architectures: a case study of the possible applications in electrochemical energy conversion. *J Alloys Compd* 706:562–567
19. Li Z, Wang C, Chen X, Wang X, Li X, Yamauchi Y, Xu X, Wang J, Lin C, Luo D, Wang X, Zhao XS (2020) MoO_x nanoparticles anchored on N-doped porous carbon as Li-ion battery electrode. *Chem Eng J* 381
20. Lim S-Y (2019) Urchin-type hollow porous structured vanadium oxide nanorod for one-dimensional lithium ion battery cathodes. *Solid State Sci* 96
21. Ren X, Liang J, Tao Z, Chen J (2011) Hydrothermal synthesis and electrochemical lithium storage performance of flower-like $NH_4V_4O_{10}$ micro/nano structures. *Chemical Journal of Chinese Universities-chinese*
22. Meng J, Zhang S, Liu X, Zhong S, Zou Z (2021) Facile synthesis of 3D urchin-like V_6O_{13} microflowers as cathode materials for high-capacity and high-rate lithium-ion batteries. *J Electroanal Chem* 900
23. Wang S, Wei W, Huang T, Zhang T, Chen Z, Chen X, Dai N (2019) Nonstoichiometric oxygen-dependent microstructures and phase transitions in post-annealed vanadium dioxides. *Adv Eng Mater* 21 (7)
24. Yi T-F, Qiu L, Qu J-P, Liu H, Zhang J-H, Zhu Y-R (2021) Towards high-performance cathodes: design and energy storage mechanism of vanadium oxides-based materials for aqueous Zn-ion batteries. *Coord Chem Rev* 446
25. Lin Y, Zhou F, Xie M, Zhang S, Deng C (2020) V_6O_{13} -delta @C nanoscrolls with expanded distances between adjacent shells as a high-performance cathode for a knittable zinc-ion battery. *ChemSuschem* 13(14):3696–3706
26. Song J, Li H, Shen H, Zhang X, Su P, Yang Y (2019) Fluoride capped V_6O_{13} -reduced graphene oxide nanocomposites: high activity oxidase mimetics and mechanism investigation. *New J Chem* 43(48):19053–19062
27. Xu S, Cen D, Gao P, Tang H, Bao Z (2018) 3D interconnected V_6O_{13} nanosheets grown on carbonized textile via a seed-assisted hydrothermal process as high-performance flexible cathodes for lithium-ion batteries. *Nanoscale Res Lett* 13(1):65
28. Zeng W, Fu X, Yu L, Shi T, Liu P, Xu J, Chen J, Qiulan C, Wang X, Xie W (2020) Growth dynamics and photoresponse of the Wadsley phase V_6O_{13} crystals. *J Mater Chem C* 8(19):6470–6477
29. Wu X, Zou Z, Li S, Zhang Y (2019) Solvothermal preparation of Ga-doped V_6O_{13} nanowires as cathode materials for lithium-ion batteries. *Ionics* 25(10):4557–4565
30. Wu X, Zou Z, Yang Q, Zhang Y (2019) Magnetic stirring assisted hydrothermal synthesis of fibrous- V_6O_{13} cathode material for lithium-ion battery. *Mater Lett* 235:176–179
31. Wang X, Ye L, Zou Y, Zhao L, Jiang Q (2021) Constructing ultra-long life and super-rate rechargeable aqueous zinc-ion batteries by integrating Mn doped V_6O_{13} nanoribbons with sulfur-nitrogen modified porous carbon. *Mater Today Energy* 19

Publisher's Note Springer Nature remains neutral with regard to jurisdictional claims in published maps and institutional affiliations.